Sensors & Diagnostics

PAPER

View Article Online
View Journal | View Issue

Cite this: *Sens. Diagn.*, 2026, **5**, 42

Electrochemically patterned biomimetic polypyrrole integrating ZnO·CuO nanoleaves for picomolar acetylcholine detection in cancer and neurological disorders

Maleeha Muhammad Din,[ab] Akhtar Hayat,[a] Shaista Ijaz Khan,[b] Palwasha Khan,[b] Mazhar Amjad Gilani,[b] Adnan Mujahid,[c] Mian Hasnain Nawaz,[a] Usman Latif*[a] and Adeel Afzal*[c]

The critical role of non-neuronal acetylcholine (ACh) as a biomarker, driving cancer proliferation and signaling neurodegenerative decline, demands sensitive, non-enzymatic diagnostic tools for early detection. This work presents a highly innovative non-enzymatic electrochemical sensor for the direct, ultra-sensitive quantification of ACh. The sensor is engineered by electropolymerizing a molecularly imprinted polypyrrole (MIP) matrix, embedded with uniquely structured ZnO·CuO nanoleaves (NLs), onto a disposable pencil graphite electrode. Computational modeling at the DFT level reveals strong non-covalent interactions that create high-fidelity recognition sites for ACh within the polymer. Comprehensive characterization (XRD, FTIR, FESEM, micro-CT, DLS) validates the successful synthesis of the nanocomposite and the precise formation of imprinting cavities. The optimized sensor achieves an exceptional detection limit of 2.2 pM and a broad linear dynamic range from 100 pM to 100 mM, ranking it among the most sensitive ACh sensors reported to date. It exhibits outstanding selectivity against key interferents and reliably detects ACh in human serum samples with excellent recovery (98.0–102.2%). This highly sensitive, robust, and cost-effective MIP-ZnO·CuO NL platform demonstrates immense potential for point-of-care clinical diagnostics in oncology and neurology.

Received 18th September 2025,
Accepted 30th October 2025

DOI: 10.1039/d5sd00169b

rsc.li/sensors

1. Introduction

Acetylcholine (ACh), the first neurotransmitter to be discovered in the early 20th century, plays a critical role in both the central and peripheral nervous systems.[1] It functions not only as a chemical messenger in the brain but also as a key modulator of numerous physiological processes, including memory, attention, movement, learning, consciousness, and sleep regulation.[2] Abnormal ACh levels have been strongly associated with a range of neurological disorders, most notably Alzheimer's disease (AD), Parkinson's disease (PD), dementia, and myasthenia gravis.[3–5] In particular, AD is characterized by a significant reduction in ACh levels, while excessive ACh concentrations can lead to symptoms such as bradycardia, excessive salivation, muscle paralysis, blurred vision, and gastrointestinal disturbances.[6,7]

The non-neuronal release of ACh has the potential to serve as an effective cancer biomarker, as it is found at elevated levels in neoplastic cells across various cancer types.[8,9] These cells significantly contribute to processes such as cell proliferation, angiogenesis, and increased invasiveness in lung, breast, colon, and gastric cancers.[10–13] Due to its central role in neurophysiology and pathology, ACh has emerged as a vital biomarker for the diagnosis, monitoring, and treatment of memory-related and neurodegenerative conditions.[3,14] Therefore, developing reliable and sensitive methods for the quantification of ACh is of growing importance in both clinical diagnostics and biomedical research.

Detection strategies for ACh are broadly categorized into direct and indirect methods. Direct approaches typically rely on the catalytic activity of nanomaterials, while indirect techniques often involve enzymatic or nanozyme-mediated reactions.[15,16] Although conventional analytical methods, such as high-performance liquid chromatography (HPLC), liquid chromatography mass spectrometry (LC-MS), and

[a] *Interdisciplinary Research Centre in Biomedical Materials (IRCBM), COMSATS University Islamabad (CUI), Lahore Campus, 54000, Pakistan. E-mail: usmanlatif@cuilahore.edu.pk*
[b] *Department of Chemistry, COMSATS University Islamabad, Lahore Campus, Pakistan*
[c] *Sensors and Diagnostics Lab, School of Chemistry, University of the Punjab, Quaid-i-Azam Campus, Lahore 54590, Pakistan. E-mail: adeel.chem@pu.edu.pk*

spectroscopic methods, have been employed for ACh quantification,[17–20] these techniques often face significant limitations. These include complex sample preparation, high operational costs, a need for skilled personnel, and a lack of suitability for real-time or point-of-care applications.

Electrochemical sensing platforms offer a promising alternative due to their simplicity, portability, cost-effectiveness, and rapid response.[1,21,22] Among these, non-enzymatic electrochemical sensors have gained increasing attention because of their robustness, operational stability across varying pH and temperature conditions, and resistance to enzyme denaturation.[21,23–25] In recent years, nanostructured materials have emerged as powerful tools in sensor development due to their high surface area, biocompatibility, ease of functionalization, and enhanced electrochemical performance.[26,27] Pencil graphite electrodes (PGEs) represent a particularly appealing option for sensor fabrication owing to their affordability, reusability, and excellent electrochemical behavior.[28,29] PGEs have shown reliable and reproducible results across multiple voltammetric techniques, making them suitable candidates for the detection of a wide range of analytes.

To further enhance specificity, molecularly imprinted polymers (MIPs) have been introduced as synthetic recognition elements.[30,31] These polymers possess tailor-made cavities complementary in shape and functional groups to the target analyte, enabling highly selective binding. Among various MIP fabrication methods, electropolymerization stands out for its ability to create stable and uniform recognition layers, with tunable characteristics governed by parameters such as scan cycles, potential window, and monomer-template ratios.[32–34]

In the present work, we report a novel non-enzymatic electrochemical sensor for ACh detection, based on the synergistic integration of ZnO·CuO nanoleaves (NLs) and polypyrrole-based MIPs on a pencil graphite electrode. The inclusion of ZnO·CuO NLs enhances the sensor's surface reactivity and selectivity due to their intrinsic electrochemical properties and affinity toward ACh.[35] The combined use of MIP and NLs enables the fabrication of a highly sensitive and selective sensor capable of detecting ACh in complex biological environments. This design offers significant potential for early diagnosis and monitoring of neurological disorders where acetylcholine plays a key biomarker role.

2. Materials and methods

2.1 Reagents and instrumentation

Chemicals such as potassium ferrocyanide, potassium ferricyanide, sodium hydroxide, zinc chloride, methanol, and acetic acid were purchased from DAEJUNG, whereas copper sulfate from SIGMA-ALDRICH, Pyrrole from TCI, acetylcholine from ChemCruz, phosphate buffer Saline (pH 7.4) from bioWorld, L-ascorbic acid from VWR chemicals, dopamine hydrochloride, L-tyrosine, and uric acid were purchased from Alfa Aesar.

Electrochemical characterizations were conducted using a Potentiostat Origa OGS 200 with a three-electrode system. The 0.5 mm PG was held using a Rotring T 0.5 pencil. Surface characterizations were performed by using a Schottky field emission scanning electron microscope (Apreo S, Thermo Fisher Scientific), and Fourier transform infrared spectroscopy (FTIR) was conducted using a Thermo Fischer Scientific spectrometer (model Nicolet 6700) to analyze the functional groups. Additionally, X-ray diffraction (XRD) analysis was performed by using a PANalytical Xpert powder diffractometer, and dynamic light scattering (DLS) measurement was accomplished using Zetasizer Nano ZS90 to outline the zeta potential and size of ZnO·CuO NLs. Micro-computed Tomography was performed by SkyScan 1272.

2.2 Synthesis of ZnO·CuO nanoleaves

Synthesis of ZnO·CuO NLs was carried out by using copper sulfate ($CuSO_4$), zinc chloride ($ZnCl_2$), and NaOH in the reaction mixture.[35] The 50 mL solution of $ZnCl_2$ was formed by adding 0.6895 g of $ZnCl_2$ to distilled water under continuous stirring. Similarly, the 50 mL solution was formed by adding 0.624 g of $CuSO_4{\cdot}5H_2O$ in distilled water under continuous stirring. After this, both solutions were mixed to prepare ZnO·CuO NLs with a volume of 100.0 mL and a pH of 4.7. The pH of the resulting mixtures was then calibrated by the addition of NaOH up to 10.34, where NLs show the best response, and the solution was then set at 90.0 °C for 6 hours of continual stirring. Later, the flask was thoroughly washed with acetone and water, and after that, kept at room temperature for 22.0 hours to allow the solvent to evaporate. The formed NLs were placed in an oven at 60 °C for 24 hours. Afterwards, these were ground and placed again in the oven at 60 °C for 22 hours. The prepared NLs can now be used for electrochemical experiments. The growth process is shown in eqn (1)–(5).

$$ZnCl_2 + 2NaOH \rightarrow Zn(OH)_2 + 2NaCl \quad (1)$$

$$Zn(OH)_2 \rightarrow ZnO(s)\downarrow + H_2O \quad (2)$$

$$CuSO_4 + 2NaOH \rightarrow Cu(OH)_2(aq) + Na_2SO_4(s) \quad (3)$$

$$Cu(OH)_2 \rightarrow CuO(s)\downarrow + H_2O \quad (4)$$

$$ZnO + CuO \rightarrow ZnO{\cdot}CuO(s)\downarrow \quad (5)$$

2.3 Electropolymerization of molecularly imprinted polypyrrole (MIP)

The fabrication of the molecularly imprinted polymer (MIP)-modified pencil graphite (PG) electrode was carried out in three sequential steps: (i) electrochemical cleaning and activation of the PG surface, (ii) electropolymerization of pyrrole (Py) in the presence of zinc oxide–copper oxide

nanoleaves (ZnO·CuO NLs) and the template molecule ACh, and (iii) removal of the embedded ACh template to generate specific recognition sites within the polymer matrix. Before electropolymerization, the PG electrode was electrochemically cleaned and activated in phosphate-buffered saline (PBS, pH 7.4) by cyclic voltammetry (CV), applying a potential range from −1.2 to +1.2 V at a scan rate of 100 mV s^{-1} until stable and reproducible voltammograms were obtained.

For the imprinting process, the electrochemical cell was loaded with 20 mL of polymerization solution containing 1 μM ACh as the template molecule, 20 mM Py as the functional monomer, and 5 μL of ZnO·CuO NLs. Electropolymerization was performed using CV over five successive cycles within a potential window of −0.6 to +1.8 V at a scan rate of 50 mV s^{-1}, resulting in the formation of an ACh-imprinted polypyrrole (PPy) film incorporating ZnO·CuO NLs on the PG surface. All solutions were prepared in PBS (pH 7.4) to maintain physiological pH conditions during synthesis. After polymerization, the ACh template was removed by using a methanol/acetic acid solution (90 : 10, v/v) under continuous stirring for 30 minutes to expose the specific binding sites within the MIP structure, enabling selective recognition of ACh in subsequent analyses. Subsequent electrochemical characterizations were conducted in a redox system comprising 0.1 M equimolar ferro/ferricyanide in 0.1 M KCl, also prepared in PBS (pH 7.4), to evaluate the electron transfer behavior and surface properties of the modified electrodes.

2.4 Computational methodology

To investigate the molecular-level interactions between the template molecule and the polymer matrix, computational modeling of the polymer–analyte complex was conducted. A trimer of polypyrrole was selected as the representative model of the polymer, and ACh was used as the target analyte. The molecular structures were modeled using GaussView 6.1.1 software.[36] The geometry optimization of all the structures was performed using Gaussian 16 software at the B3LYP-D3/6-311 ++ G (d.p) level of theory.[37] The interaction energy (ΔE) of the polymer–analyte complexes was computed by using the following equation:

$$\Delta E = E_{\text{complex}} - (E_{\text{analyte}} + E_{\text{polymer}}) \quad (6)$$

where ΔE represents the total energy, E_{analyte} is the energy of the analyte, E_{polymer} represents the energy of the polymer, and E_{complex} represents the energy of the complex. The bonding parameters were analyzed by QTAIM (quantum theory of atoms in molecules) analysis.[2] The interaction region indicator (IRI) analysis was performed to identify the type of interactions between the polymer and the analyte. Both analyses were performed using Multiwfn[38] and visualized by VMD (Visual Molecular Dynamics) software.[39]

3. Results and discussion

3.1 Characterization

The successful synthesis of ZnO·CuO NLs and the subsequent fabrication of the MIP electrode were confirmed through multiple analytical techniques. The crystalline structure and phase purity of the synthesized ZnO·CuO NLs were first ascertained by XRD. The diffraction pattern (Fig. 1a) exhibited characteristic peaks indexed to the wurtzite structure of ZnO (JCPDS no. 36-1451;[40] peaks (100), (002), (110)) and the monoclinic phase of CuO (JCPDS no. 48-1548;[41] peaks (111), (200)), confirming the formation of a composite without intermediate phases.

FTIR spectroscopy (Fig. 1b) further validated the chemical composition.[3] The broad absorption band at ∼3423 cm^{-1} is attributed to O–H stretching vibrations from surface-adsorbed water.[42] The peaks at 1414 and 1099 cm^{-1} may correspond to residual carbonaceous species or carbonate groups,[43] while the distinct metal–oxygen vibrations for Zn–O and Cu–O were observed below 700 cm^{-1}. The optical properties of the NLs were probed by UV-vis spectroscopy (Fig. 1c), which showed a broad absorption profile spanning 300–800 nm. This is indicative of charge-transfer processes and the presence of defect states within the ZnO·CuO heterojunction, which are crucial for its electrocatalytic activity.[44]

Dynamic light scattering (DLS) was used to analyze the hydrodynamic size and colloidal stability of the ZnO·CuO NLs. The NLs exhibited an average hydrodynamic diameter of ∼1063 nm and a near-neutral zeta potential of +0.02 mV (Fig. 1d). The high polydispersity index (PDI = 0.8) indicates a broad size distribution, which is consistent with the observed nanoleaves morphology that can vary in dimensions. Finally, the morphology of ZnO·CuO was examined by FE-SEM. As shown in Fig. 1e, the synthesized material exhibited a distinct leaf-like morphology with a high surface area, which is advantageous for facilitating electron transfer and providing ample sites for polymer functionalization.

The successful modification of the pencil graphite (PG) electrode surface was tracked by FE-SEM and X-ray microcomputed tomography (micro-CT). Micro-CT analysis provided complementary insights into the internal density distribution of the electrode. The bare PG electrode exhibited low density and high X-ray transmissivity (Fig. 1f). In contrast, the MIP-modified electrode (ACh + $PPy(NLs)_{imp}$/PG) showed a significantly denser structure, confirming the successful incorporation of the polypyrrole matrix and ZnO·CuO NLs throughout the electrode volume (Fig. 1g).

The bare PG electrode showed a heterogeneous surface of graphite and clay particles (Fig. 1h). Following electropolymerization in the presence of the template (ACh) and NLs (TP + PPy(NLs)/PG), a rough, composite layer was observed, confirming successful deposition (Fig. 1i). Subsequent template removal ($PPy(NLs)_{imp}$/PG) resulted in a smoother surface morphology, consistent with the creation of

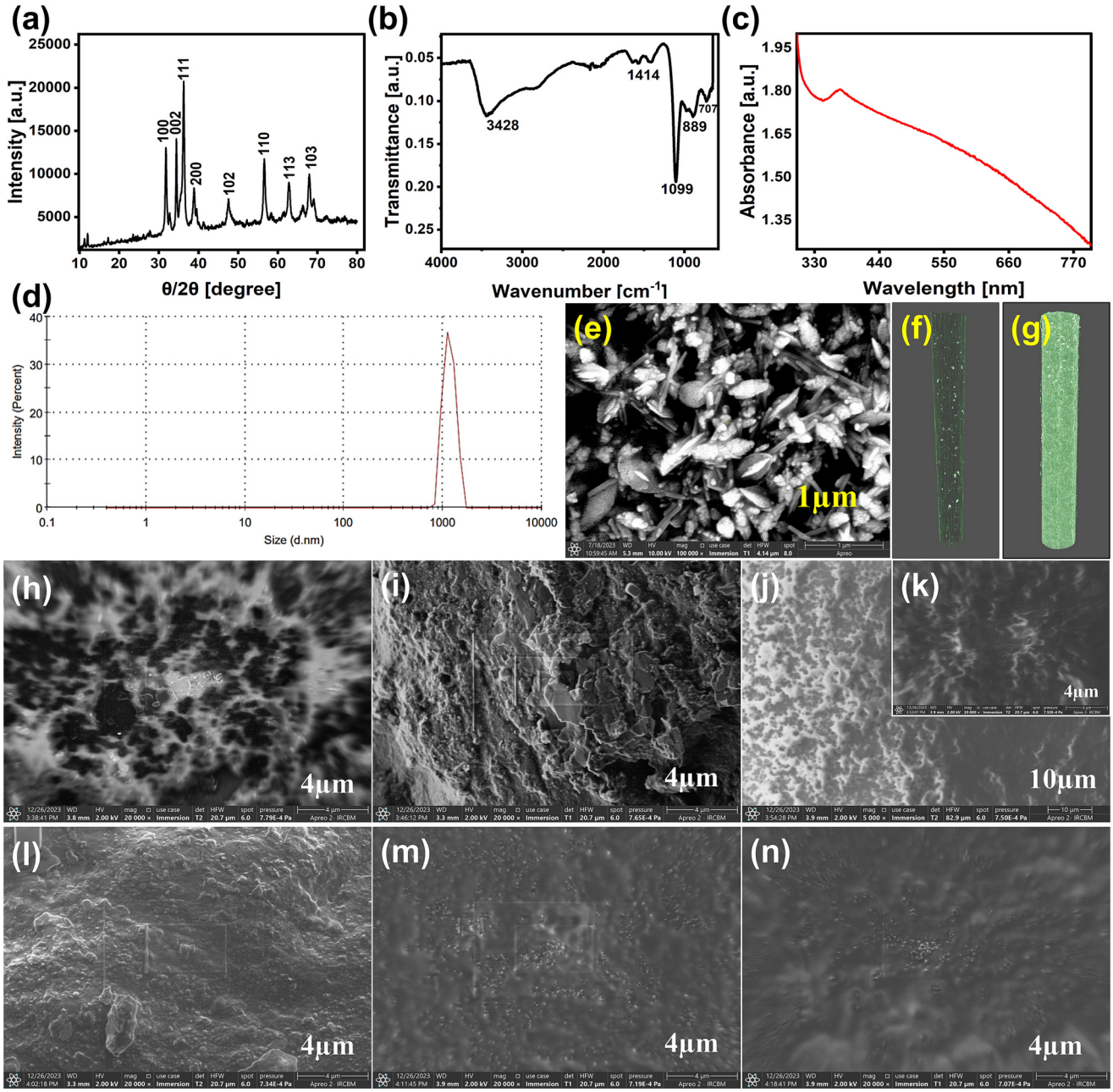

Fig. 1 Comprehensive physicochemical characterization of ZnO·CuO NLs and modified electrode surfaces. (a) XRD pattern confirming the crystalline phases of wurtzite ZnO and monoclinic CuO. (b) FTIR spectrum of ZnO·CuO NLs. (c) UV-vis absorption spectrum showing a broad absorption band. (d) DLS analysis showing the hydrodynamic size distribution of the ZnO·CuO NLs. (e) FESEM image revealing the nanoleaves morphology of the synthesized ZnO·CuO. Micro-CT images showing the density distribution of (f) bare PG and (g) the MIP-modified electrode (ACh + $PPy(NLs)_{imp}$/PG). FESEM images of electrode surfaces at each modification step: (h) bare PG electrode, (i) after electropolymerization with template (TP + PPy(NLs)/PG), (j) after template removal ($PPy(NLs)_{imp}$/PG), with a higher magnification image (k) shown in the inset (l) after rebinding with ACh (ACh + $PPy(NLs)_{imp}$/PG), (m) non-imprinted polymer electrode ($PPy(NLs)_{non\text{-}imp}$/PG), and (n) non-imprinted electrode after ACh exposure (ACh + $PPy(NLs)_{non\text{-}imp}$/PG).

molecular cavities (Fig. 1j and k). Re-exposure to ACh led to a reappearance of surface roughness, confirming successful rebinding into the imprinted sites (Fig. 1l). In contrast, the non-imprinted polymer (NIP) electrode ($PPy(NLs)_{non\text{-}imp}$/PG) remained smooth before (Fig. 1m) and after incubation with ACh, with only non-specific aggregation noted (Fig. 1n), emphasizing the specificity of the MIP.

3.2 Fabrication and electrochemical characterization

The fabrication and molecular imprinting mechanism are schematically illustrated in Fig. 2a. During the electropolymerization process (Fig. 2a), the oxygen atom in ACh forms hydrogen bonds with the N–H group of the pyrrole monomers. The chloride ion of ACh may also engage

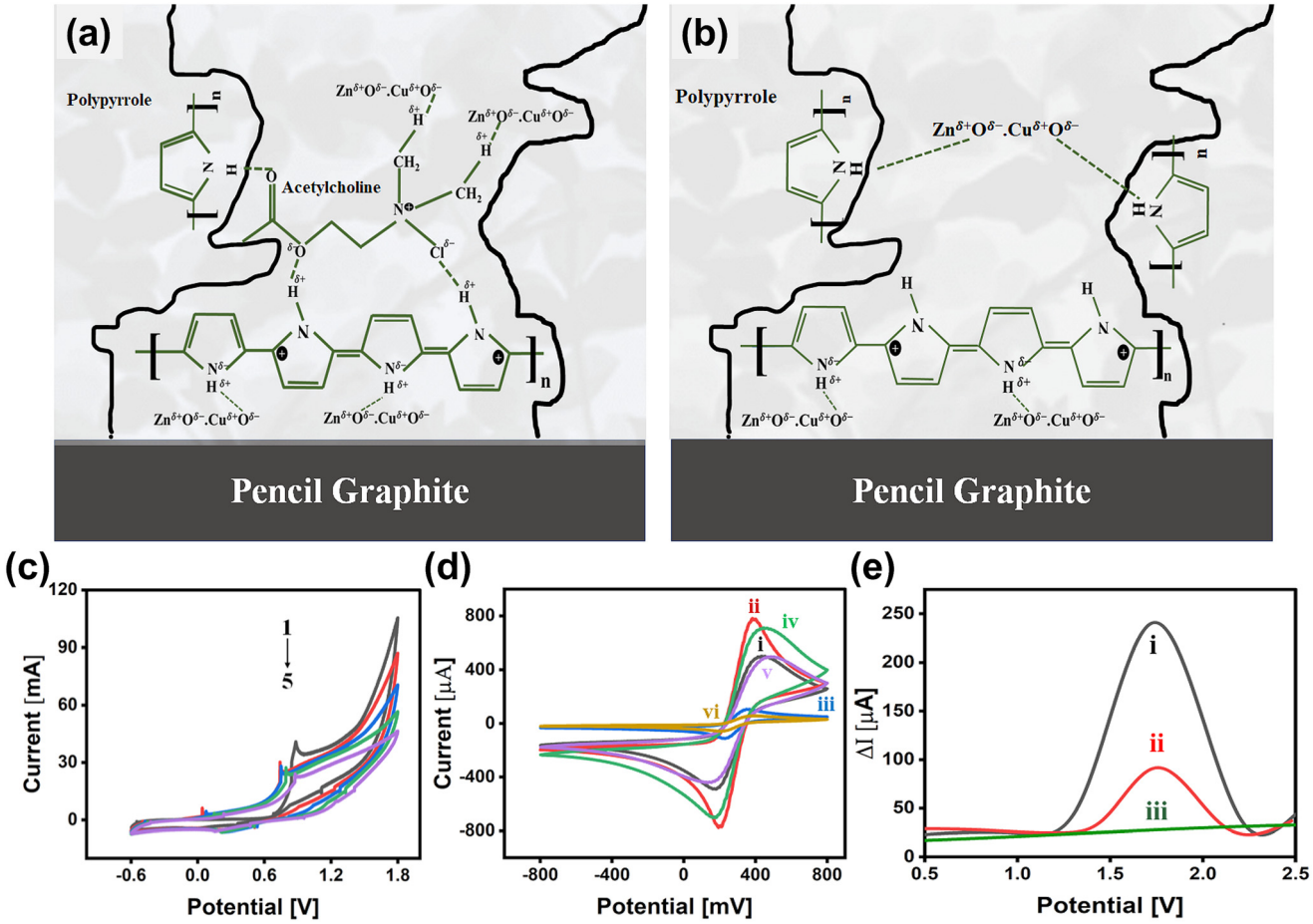

Fig. 2 Schematic illustration of the proposed molecular imprinting and recognition process: (a) co-assembly of pyrrole monomer, ACh template, and ZnO·CuO NLs during electropolymerization, and (b) subsequent template removal to create specific recognition cavities, showing the chemical interactions between PPy, ACh, and the NLs. Electrochemical characterization: (c) cyclic voltammograms recorded during the electropolymerization of pyrrole on the PG electrode over five cycles, showing the progressive formation of the PPy film in the presence of ACh and ZnO·CuO NLs. (d) CV responses of the modified electrodes in a 0.1 M $[Fe(CN)_6]^{3-/4-}$ redox probe: (i) bare PG, (ii) after electropolymerization with template and ZnO·CuO NLs (TP + PPy(NLs)/PG), (iii) after template removal ($PPy(NLs)_{imp}$/PG), (iv) after rebinding with ACh (ACh + $PPy(NLs)_{imp}$/PG), (v) non-imprinted polymer electrode ($PPy(NLs)_{non\text{-}imp}$/PG), and (vi) non-imprinted electrode after ACh incubation (ACh + $PPy(NLs)_{non\text{-}imp}$/PG). (e) Differential pulse voltammetry (DPV) responses highlighting the recognition performance: (i) MIP after ACh rebinding, (ii) MIP after template removal, and (iii) NIP after ACh exposure.

in electrostatic or hydrogen bonding interactions with the pyrrole backbone. Crucially, the ZnO·CuO NLs participate through their surface oxygen species in additional hydrogen bonding and electrostatic interactions, further stabilizing the template during imprinting. These multi-faceted interactions create well-defined recognition sites that mimic the spatial and chemical functionality of ACh. After polymerization, the embedded ACh template was removed (Fig. 2b) using a methanol/acetic acid solution (90 : 10, v/v) to generate the specific cavities, followed by a PBS wash to neutralize residual acid.

The electropolymerization of pyrrole onto the PG electrode in the presence of ACh and ZnO·CuO NLs was monitored *via* CV (Fig. 2c). A distinct oxidation peak appeared during the first scan, indicating the oxidative polymerization of pyrrole and the concurrent entrapment of the ACh template. As the number of scans increased, the oxidation peak current gradually decreased, reaching a plateau after five cycles. This trend confirms successful film formation and is attributed to the growing thickness of the PPy film, which progressively impedes monomer diffusion and electron transfer. Although ACh itself is not electrochemically redox-active, its incorporation is essential as a structural template, guiding polymer growth *via* non-covalent interactions to form specific imprint sites and influencing the polymer morphology for efficient charge transport.

During electropolymerization, pyrrole is oxidized to radical cations that couple into a conductive PPy matrix, entrapping ACh and forming template-specific cavities near ZnO·CuO sites. After template removal, these sites selectively rebind ACh, which undergoes anodic oxidation to yield choline and acetate, producing the DPV signal. ZnO·CuO nanoleaves assist imprint formation through surface hydroxyl and Lewis-acidic centers and catalyze electron transfer by stabilizing

intermediates and reducing overpotential, while the PPy network ensures conductivity and structural stability.

$$\text{Pyrrole} \rightarrow \text{pyrrole}^{\bullet} + (\text{polymerization}) \rightarrow (\text{PPy})_n^{+} + ne^{-} + nH^{+} \quad (7)$$

$$\text{ACh}_{(aq)} \rightleftharpoons \text{ACh}_{ads} \quad (8)$$

$$\text{ACh}_{ads} \rightarrow \text{ACh}_{ads}^{\bullet+} + e^{-} \quad (9)$$

The electron transfer characteristics at each stage of electrode modification were evaluated using a 0.1 M $[Fe(CN)_6]^{3-/4-}$ redox probe, with the CV responses presented in Fig. 2d.

The bare PG electrode (Fig. 2d-i) exhibited a well-defined redox peak. After electropolymerization with the template and ZnO·CuO NLs (TP + PPy(NLs)/PG, Fig. 2d-ii), an increase in peak current was observed, attributed to the improved conductivity and surface area from the incorporated NLs and the initial embedding of ACh. Following template removal ($(PPy(NLs)_{imp}/PG$, Fig. 2d-iii), a noticeable reduction in peak current confirmed successful extraction of ACh and the creation of insulating cavities. Upon rebinding ACh (ACh + $PPy(NLs)_{imp}/PG$, Fig. 2d-iv), the peak current increased again, indicating the effective re-adsorption of the target analyte into the imprinted cavities.

The incorporation of ZnO·CuO NLs markedly enhances sensor performance. These nanoleaves contribute both electrocatalytically and chemically. Their n–p heterojunction facilitates charge separation, reducing resistance and amplifying analyte-specific signals. Surface oxygen groups of ZnO·CuO stabilize the ACh template during polymerization through hydrogen bonding, yielding well-defined cavities. Comparative CV data (Fig. 2d) show that removing NLs markedly diminishes response, validating their unique role in selectivity enhancement.[45] Additionally, their high surface area, electroactive nature, and the synergistic electronic properties of the ZnO·CuO binary system (combining ZnO's high electron mobility with CuO's p-type conductivity)[46,47] lower the internal resistance of the MIP layer. This results in faster electron transfer kinetics, manifesting as an enhanced current response. Furthermore, their nanoleaves' morphology, characterized by high porosity, increases the active surface area, improving analyte accessibility and acting as nanoelectrocatalysts to accelerate signal transduction.

In stark contrast, the non-imprinted polymer electrode ($PPy(NLs)_{non\text{-}imp}/PG$, Fig. 2d-v) showed a reduced current, and its response after ACh incubation (ACh + $PPy(NLs)_{non\text{-}imp}/PG$, Fig. 2d-vi) showed only a minor change, highlighting the lack of specific recognition sites and validating the successful imprinting effect. To further evaluate the recognition performance, DPV was conducted (Fig. 2e). A strong DPV response was observed after rebinding ACh to the MIP electrode (Fig. 2e-i), confirming the effective occupation of the imprinted cavities. A decreased signal was seen after template removal (Fig. 2e-ii), consistent with empty cavities. The NIP electrode after ACh exposure (Fig. 2e-iii) showed a minimal response, reinforcing its inability to selectively bind the target analyte. These results collectively confirm that the MIP-modified electrode provides a tailored microenvironment with high selectivity for ACh.

3.3 Optimization of the electrodes

The analytical performance of the MIP sensor is critically dependent on the nanoscale architecture and physicochemical properties of the imprinted layer. We systematically optimized key fabrication parameters to maximize sensitivity and selectivity by precisely balancing recognition site density, analyte diffusivity, and electron transfer efficiency. Monomer and template concentrations govern the fidelity and accessibility of molecular recognition sites. A pyrrole concentration of 60 mM yielded an optimal response (Fig. 3a), providing sufficient monomer for a robust, cavity-rich film. Higher concentrations lead to an overly dense and thick polymer matrix, which acts as a kinetic barrier, severely impeding analyte diffusion to the underlying electrode and hindering electron transfer. Similarly, the template (ACh) concentration of 100 μM maximized signal (Fig. 3b), facilitating the formation of optimal pre-polymerization complexes for a high density of well-defined and specific cavities.

The ZnO·CuO NLs loading was optimized to use their synergistic electrocatalytic and conductive properties without compromising film integrity. An 8 mg loading maximized the electrochemical response (Fig. 3c). At this loading, the ZnO·CuO NLs provide maximal surface area for polymer nucleation, enhance charge transport through the formation of conductive pathways, and likely participate in stabilizing the template-monomer complex. Beyond this optimum loading, performance declined precipitously, a consequence of ZnO·CuO NL agglomeration, which disrupts polymer homogeneity, blocks pore networks, and creates insulating regions that hinder efficient charge transfer. Electropolymerization cycles directly control film thickness and morphology. 10 CV cycles were found to be optimal (Fig. 3d), producing a film with a high density of imprinted cavities while maintaining efficient mass transport and electron transfer kinetics. Fewer cycles result in incomplete and unstable surface coverage, whereas excessive cycling forms a thick, tortuous layer that introduces significant diffusional limitations for the analyte and the redox probe.

Finally, the template removal and analyte rebinding kinetics were quantified to ensure functional cavity generation. A 30 minute extraction in methanol/acetic acid (90 : 10 v/v) was sufficient for complete template removal and the generation of accessible, high-fidelity cavities (Fig. 3e). Rebinding equilibrium was achieved within 40 minutes (Fig. 3f), confirming efficient mass transport into the porous MIP network and saturation of the specific recognition sites without significant contribution from non-specific adsorption, as corroborated by the NIP control. This optimized protocol ensures the fabrication of a highly functional MIP interface with maximal analyte recognition

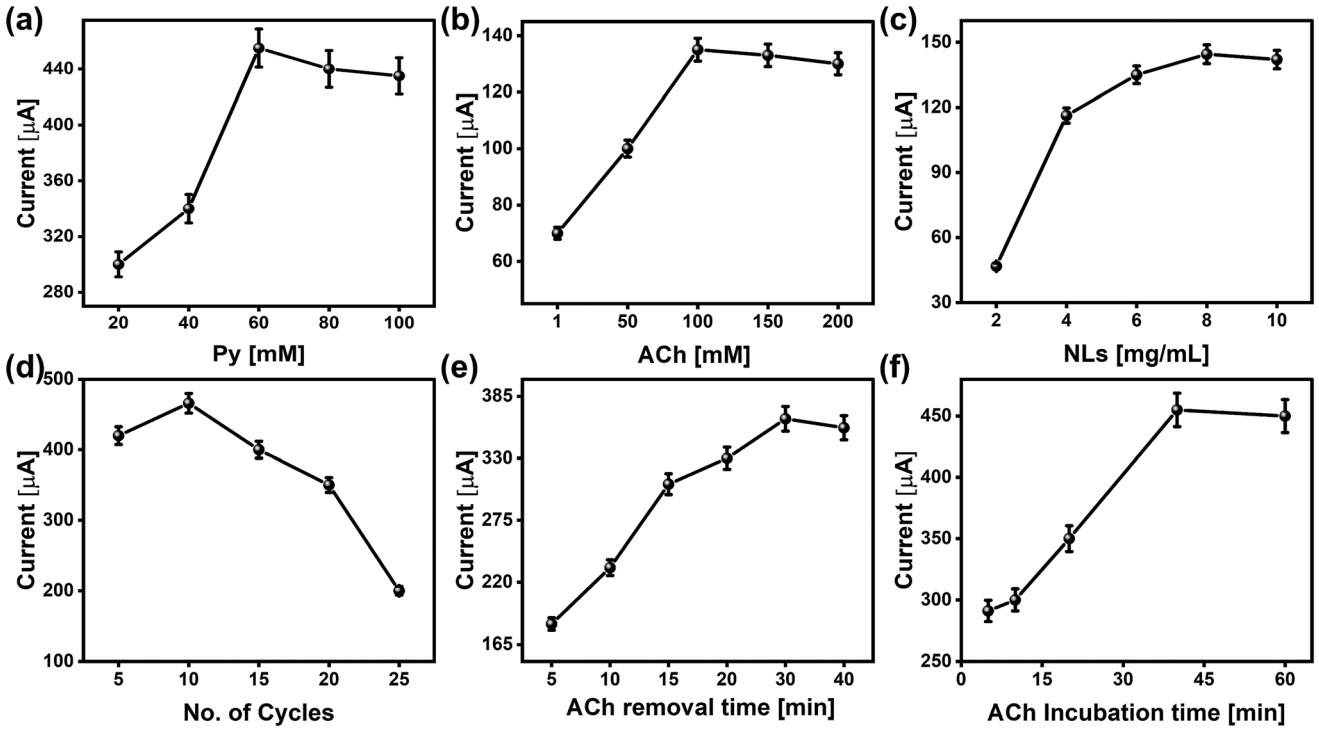

Fig. 3 Optimization of experimental parameters. Effect of varying: (a) pyrrole monomer concentration, (b) acetylcholine (ACh) template concentration, (c) ZnO·CuO NLs concentration, (d) number of electropolymerization cycles, (e) template removal time, and (f) ACh rebinding time on the sensor's peak current response.

capability and electrochemical signal amplification for ultrasensitive detection.

3.4 Redox mechanism and recognition events

To elucidate the electron transfer mechanism and the effectiveness of the molecular imprinting process, we systematically characterized each stage of electrode modification using CV with the standard $[Fe(CN)_6]^{3-/4-}$ redox probe. CV performed across scan rates (10–100 mV s^{-1}) revealed a linear relationship between the peak current (I_p) and the square root of the scan rate ($v^{1/2}$) for all electrodes (Fig. 4a–f), indicating that the electrochemical process is predominantly diffusion-controlled.[48,49] Furthermore, the analysis of the peak potential separation (ΔE_p) confirmed quasi-reversible electron transfer kinetics *via* linear fit of ΔE_p *versus* scan rate (Fig. 4a–f, insets),[50] establishing a baseline for comparing interfacial changes induced by surface modifications.

A more quantitative assessment was achieved by calculating the electroactive surface area (A) for each electrode configuration using the Randles–Ševčík equation.[51] The calculated area for the bare GP electrode (0.00203 cm^2) served as a fundamental reference. The sequence of area changes provides a compelling narrative of the imprinting and rebinding events:

A significant reduction in electroactive area to 0.00047 cm^2 for the templated polymer electrode (TP + PPy(NLs)/PG) is a clear indicator of successful electropolymerization. The forming polypyrrole matrix, embedded with ACh template molecules, acts as an insulating layer, severely hindering the diffusion of the redox probe to the underlying electrode surface and dramatically reducing the available area for electron transfer.

Following the extraction of the ACh template ($PPy(NLs)_{imp}$/PG), the electroactive area not only recovered but also increased to 0.00309 cm^2. This result is critical and suggests that the removal process does more than just create cavities; it likely enhances surface roughness and exposes the conductive moieties of the embedded ZnO·CuO NLs, thereby creating new, efficient electron transfer pathways within the porous MIP architecture.

The rebinding of ACh molecules (ACh + $PPy(NLs)_{imp}$/PG) caused a measurable decrease in the active area to 0.00285 cm^2. This observation is a direct electrochemical signature of the molecular recognition event. The target analytes selectively reoccupy the imprinted cavities, partially obstructing the access of the $[Fe(CN)_6]^{3-/4-}$ ions to the conductive surface and thus modulating the current response. The final decrease to 0.00203 cm^2 upon further rebinding confirms the high affinity and capacity of the cavities for ACh, effectively returning the accessible surface to a state akin to the original blocked surface.

This sequence of area change, *i.e.*, blocking, opening, and selective re-blocking, is a powerful validation of the MIP's functionality. In stark contrast, the NIP electrode showed a

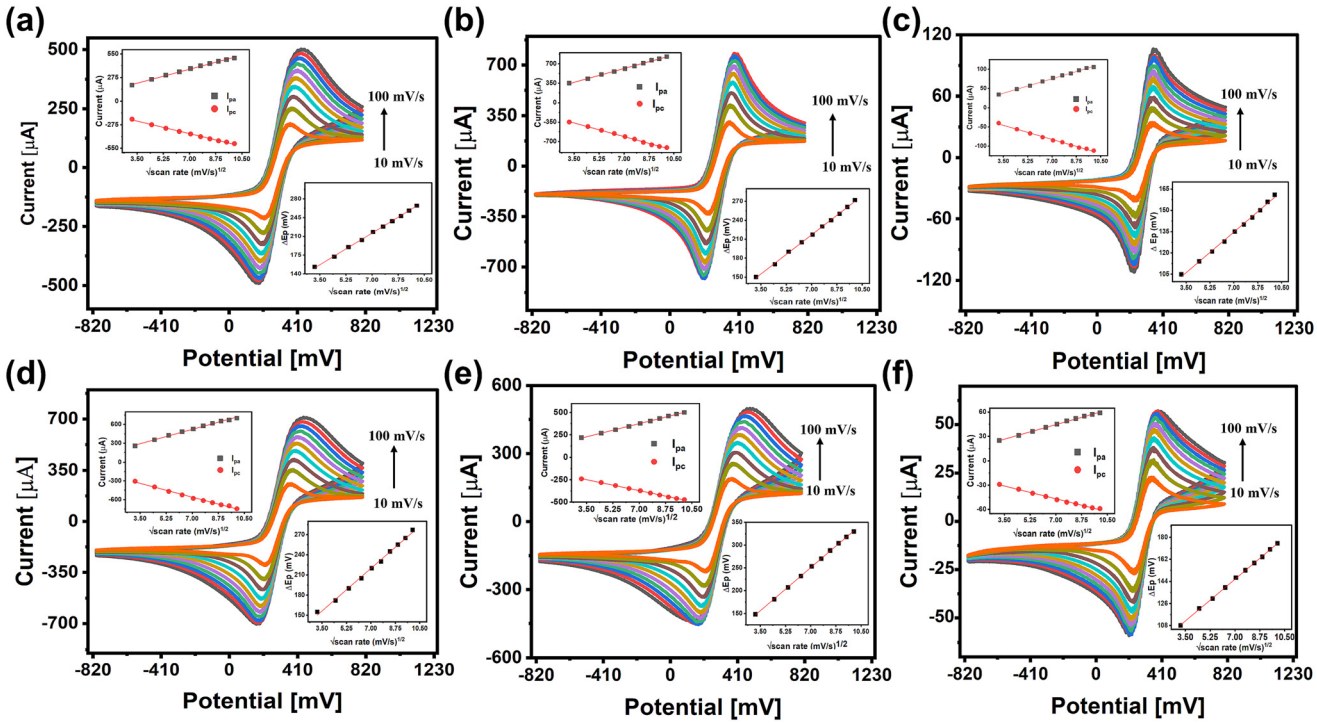

Fig. 4 Electrochemical kinetics study. Cyclic voltammograms of (a) bare PG, (b) TP + PPy(NLs)/PG, (c) PPy(NLs)$_{imp}$/PG, (d) ACh + PPy(NLs)$_{imp}$/PG, (e) PPy(NLs)$_{non\text{-}imp}$/PG, and (f) ACh + PPy(NLs)$_{non\text{-}imp}$/PG in a 0.1 M $[Fe(CN)_6]^{3-/4-}$ solution at varying scan rates (10–100 mV s^{-1}). The linear dependence of peak current (I_p) on the square root of scan rate and peak separation (ΔE_p) on the scan rate (insets) confirms a diffusion-controlled quasi-reversible process for all electrode configurations.

moderate reduction in area (0.00183 cm^2) due to non-specific polymer coverage, followed by a catastrophic collapse to 0.00022 cm^2 after incubation with ACh. This drastic, irreversible reduction indicates non-specific adsorption and surface fouling, a common drawback of non-selective polymers that leads to passivation. The stark divergence between the MIP and NIP responses emphasizes the precision of the imprinting strategy. The MIP exhibits a controlled, analyte-specific, and reversible modulation of interface properties, directly linked to binding events within well-defined cavities.

3.5 Analytical performance: ultrasensitive and wide-range detection

The analytical efficacy of the ACh-imprinted sensor was quantitatively evaluated using the highly sensitive technique of DPV. The sensor exhibited a remarkable and concentration-dependent response to acetylcholine across an exceptionally wide dynamic range, from 100 pM to 100 mM, *i.e.*, spanning an unprecedented twelve orders of magnitude (Fig. 5a). This range comprehensively covers the pathophysiological concentrations of ACh found in both neurological environments and oncological contexts. A well-defined oxidation peak current increased systematically with each increment in ACh concentration. Plotting the peak current against the logarithm of concentration yielded a linear calibration curve with an excellent coefficient of determination (R^2 = 0.998), confirming a robust and predictable sensor response across this vast concentration spectrum (Fig. 5b). The slope of this curve corresponds to a high sensitivity (~18.4 ± 0.5 μA/log[Ach(pM)]), which is attributed to the synergistic electrocatalysis of the ZnO·CuO NLs and the high density of specific recognition sites within the molecularly imprinted cavities that facilitate efficient binding and signal transduction.

The sensor demonstrated exceptional sensitivity (~18.4 ± 0.5 μA/log[Ach(pM)]), with a calculated limit of detection (LOD) of 2.2 pM and a limit of quantification (LOQ) of 7.3 pM. LOD and LOQ were calculated using standard equations (LOD = $3\sigma/S$; LOQ = $10\sigma/S$) with σ from n = 3 replicates.[52,53] This ultra-low LOD, coupled with the vast dynamic range, positions this sensor among the most sensitive ACh detection platforms ever reported (see comparative Table 1). The calibration profile remained stable across the entire range, with minimal deviation observed only at the highest concentrations (≥10 mM), a phenomenon consistent with analyte saturation and diffusional limitations in the densely packed binding sites. This performance underscores the sensor's unique capability for reliable quantification of ACh in both trace-level and high-concentration environments, a critical requirement for its application in complex and variable biological matrices such as serum, cerebrospinal fluid, or tumor microenvironments.

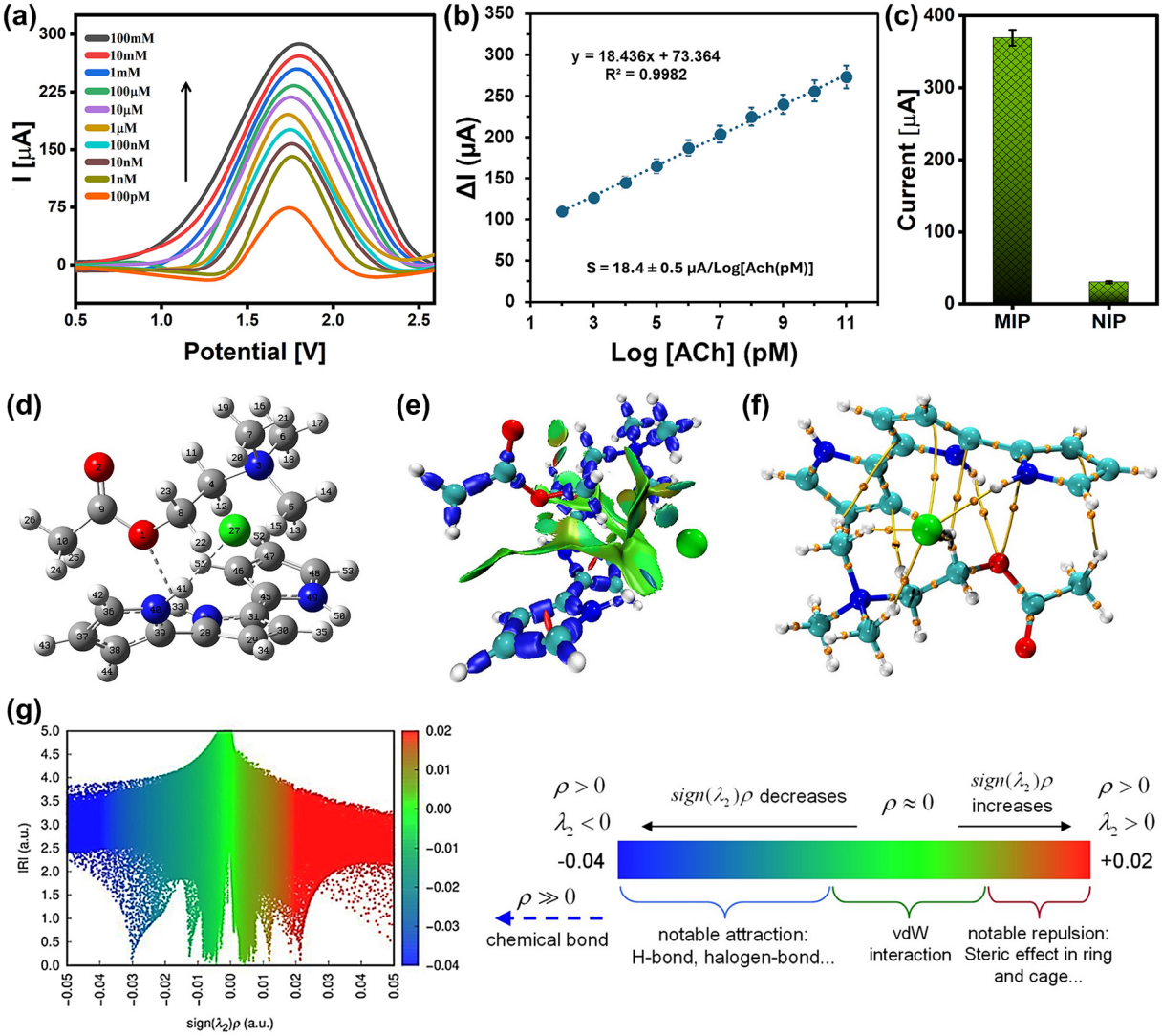

Fig. 5 Analytical performance. (a) DPV responses for ACh concentrations from 100 pM to 100 mM, (b) the corresponding calibration curve of peak current *vs.* logarithm of concentration, (c) comparison of the MIP response to ACh against the NIP response. Computational analysis of the ACh–PPy complex: (d) optimized geometry of the ACh–polypyrrole trimer complex, (e) interaction region indicator (IRI) isosurface (blue indicates strong attractive interactions), (f) quantum theory of atoms in molecules (QTAIM) analysis showing bond critical points (BCPs, small red spheres) and bond paths, (g) IRI scatter plots visualizing the nature and strength of non-covalent interactions within the complex.

3.6 Computational validation of molecular recognition

Computational modeling at the DFT-D3 level of theory was employed to decipher the molecular-level interactions governing the high selectivity of the MIP,[54] providing an atomistic rationale for the observed sensor performance. A systematic conformational search was performed to identify the most stable complexation mode between a PPy oligomer (representing the polymer matrix) and ACh. The identified global minimum configuration, with a significant interaction energy of −23.0 kcal mol^{-1}, confirms the thermodynamic feasibility of spontaneous, exothermic binding and the formation of a highly stable complex (Fig. 5d).

The nature and strength of this interaction were elucidated through a multi-faceted topographical analysis. The geometry-optimized structure revealed two key intermolecular contacts. Calculated bond critical point (BCP) distances of 2.21 Å and 2.36 Å between the N–H group of the pyrrole ring and the chloride anion (Cl$^-$) and ester oxygen (O) atoms of ACh, respectively, are characteristic of moderate-strength hydrogen bonds. This was further confirmed by interaction region indicator (IRI) analysis,[55] where the distinct blue isosurfaces and a pronounced peak at −0.04 a.u. in the scatter plots between these atoms provide visual and quantitative evidence of strong, attractive non-covalent interactions, with no significant repulsive (red) character observed (Fig. 5e–g).

A full topological analysis *via* the QTAIM provided definitive insight into the electronic structure and bond character.[54,56] The electron density (ρ) at the BCPs was found to be greater than 0.01 au but less than the 0.1 au threshold

Table 1 Performance comparison of selected electrochemical sensors for acetylcholine (ACh) detection

Composition of the electrodes	LOD (μM)	Linear range (μM)	Ref.
ZnO·CuO NLs/nafion	14.7 pM	100 pM–100 mM	35
NiAL-LDHs	1.7 μM	5–6885 μM	58
AChE-ChO/cPPy-PVS	5.0 nM	10 nM–1 μM	59
AChE-ChO/PtNPs-GO/ITO	0.005 μM	0.005–700 μM	60
Fe_2O_3NPs/rGO/PEDOT	4 nM	4 nM–800 μM	61
AChE/ZnS/ZnO/Ta_2O_5–SiO_2/GCE	11.6 nM	100 nM–1200 μM	62
AChE-ChO/PtNPs/MOF/Au	0.01 μM	0.01–500 μM	63
AChE-ChO/MWCNT-MnO_2/rGO/Au	0.1 μM	0.1–100 μM	64
MCPE (NiO NSs CPE)	26.7 μM	0.25–5.88 mM	65
$ZnFe_2O_4$/SPE	0.024 μM	0.08–500 μM	66
Nitrogen ion-implanted WO_3/ITO	28 nM	0.1–8000 μM	67
Cu@Cu_2O-BNDC	17 nM	0.3–2602 μM	68
$CuCo_2O_4$ nanoplates	30 nM	0.2–3500 μM	69
CuMS@C	0.1 μM	0.01–0.8 mM	70
GCE/V_2O_5 NRs/BPM	11.58 pM	100 pM–100 μM	71
MIP-PPy(CuO·ZnO NLs)/PG	**2.2 pM**	**100 pM–100 mM**	**This work**

Table note. LOD: limit of detection; ITO: indium tin oxide; NiAl: nickel aluminum; LDHs: layered double hydroxides; WO_3: tungsten trioxide; V_2O_5: vanadium pentoxide nanorods; CuMS@C: carbon-doped Cu-microspheres; PPM: binding polymer matrix; PG: pencil graphite electrode; MCPE: modified carbon paste electrode; GCE: glassy carbon electrode; rGO: reduced graphene oxide; BNDC: B and N co-doped mesoporous carbon; SPE: screen printed electrode.

typical of covalent bonds, placing these interactions firmly in the non-covalent regime. The positive values for the Laplacian of the electron density ($\nabla^2\rho > 0$) at these points confirm a depletion of electron density at the BCP,[57] which is a key topological signature of electrostatic-dominant, closed-shell interactions such as hydrogen bonding. However, the slightly negative total energy density ($H_r < 0$) suggests these hydrogen bonds have a non-negligible degree of electron sharing or covalency, classifying them as particularly strong and stabilizing interactions that are essential for effective and specific molecular recognition. This nuanced electronic structure, a hybrid of electrostatic and partial covalent character, provides a robust theoretical foundation for the excellent binding affinity and selectivity observed experimentally.

The remarkable consistency between the computational prediction of strong, specific hydrogen bonding and the experimental results, exceptional rebinding efficiency, and an ultra-low detection limit, provides a fundamental atomistic validation of our sensor's design principle. The computations confirm that the MIP cavities are not merely sterically complementary voids but are functionally tailored with precisely positioned chemical groups that engage the target analyte *via* optimal, multi-point hydrogen bonding. This powerful synergy between theoretical modeling and experimental validation highlights the role of computation not just as a supporting tool, but as a critical component in the rational design of advanced molecular recognition interfaces.

3.7 Selectivity and anti-interference performance

The deployment of electrochemical sensors in complex biological matrices is contingent upon their ability to discriminate the target analyte against a background of structurally similar and electroactive interferents. To rigorously evaluate this critical parameter, the ACh-imprinted sensor was challenged with a solution of 10 nM acetylcholine spiked with high concentrations (100 nM) of common endogenous interferents: acetylcholinesterase, ascorbic acid, tyrosine, dopamine, uric acid, and glucose. As quantified in Fig. 6a, the sensor exhibited a pronounced and unambiguous response to acetylcholine. Crucially, the subsequent introduction of each interferent, at a ten-fold excess, induced only a negligible perturbation in the amperometric signal, with all variations remaining within a strict ±3.5% margin of the original ACh response. This exceptional selectivity profile is a direct consequence of the molecular imprinting strategy, which creates synthetic recognition cavities with a precise stereochemical and chemical complementarity to ACh. These cavities facilitate specific binding through optimal hydrogen bonding and electrostatic interactions, as validated by our computational models, while effectively excluding larger or differently shaped molecules. The demonstrated anti-interference capability, particularly against common redox-active species that typically plague electrochemical detection, underscores a significant advantage of this non-enzymatic, biomimetic approach. It confirms that the sensor's performance is governed by specific molecular recognition rather than non-specific adsorption or surface electrocatalysis. This high degree of specificity is a fundamental prerequisite for the reliable and accurate quantification of ACh in complex clinical samples such as serum, cerebrospinal fluid, or tumor microenvironment aspirates, where the analyte of interest is surrounded by a multitude of confounding species.

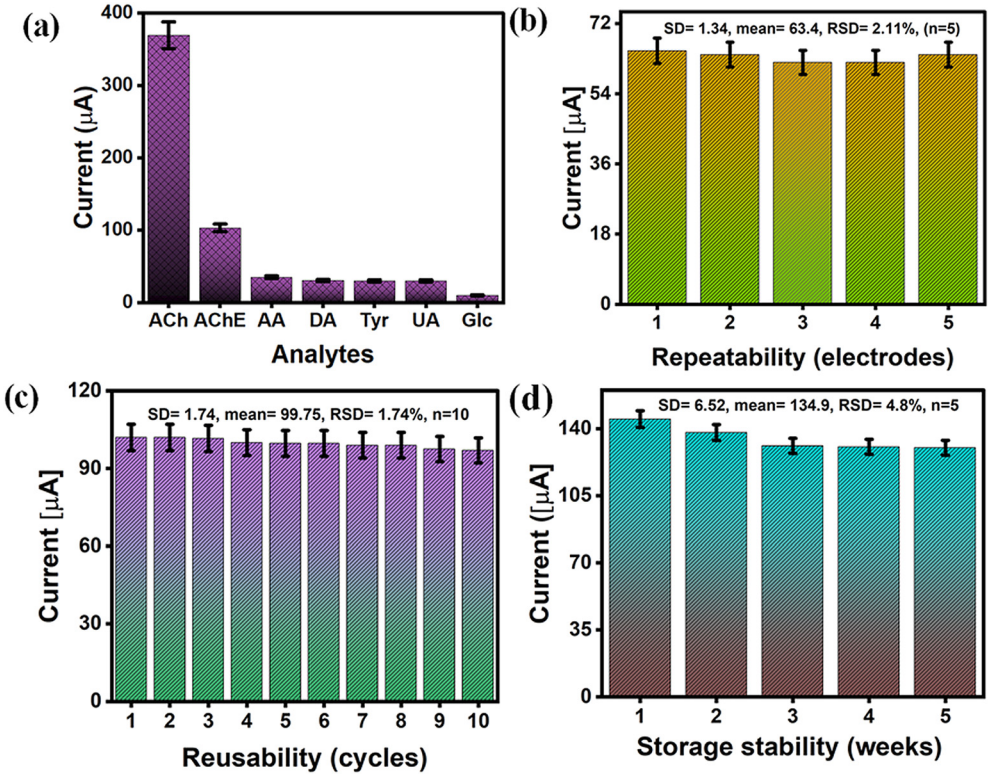

Fig. 6 Assessment of sensor robustness and reliability: (a) selectivity study of the MIP sensor against acetylcholine (ACh), acetylcholine esterase (AChE), ascorbic acid (AA), dopamine (DA), tyrosine (Tyr), uric acid (UA), and glucose (Glc), (b) repeatability across five independently fabricated electrodes, (c) reusability over 10 cycles of template removal and rebinding, and (d) storage stability over five weeks.

3.8 Robustness: repeatability, reusability, and stability

The transition of a sensing technology from a laboratory prototype to a practical analytical tool is predicated on its robustness under operational conditions. ACh-imprinted sensor is rigorously evaluated across three critical metrics: repeatability, long-term stability, and reusability. Repeatability is a cornerstone of reliable manufacturing and measurement. To quantify this, five independent sensors were fabricated in separate batches under identical optimal conditions. When challenged with a 100 μM ACh solution, the electrochemical response across all five electrodes exhibited remarkable consistency, yielding a low relative standard deviation (RSD) of 2.11% (Fig. 6b). This minimal batch-to-batch variation confirms the high precision and controllability of the electropolymerization and imprinting process, which is essential for the scalable production of dependable sensors.

Reusability represents a significant economic and operational advantage over single-use sensors. The sensor could be efficiently regenerated *via* a simple template elution protocol and subjected to ten consecutive cycles of measurement and regeneration. Throughout this rigorous process, the sensor maintained its performance with a signal attenuation of less than 5% (Fig. 6c). This demonstrates not only the mechanical robustness of the nanocomposite film against repeated electrochemical cycling and chemical treatment but also the fully reversible nature of the ACh binding process within the imprinted cavities. Fresh pencil graphite electrodes (PGEs) were used for each modification and measurement to ensure reproducibility. All experiments were conducted in triplicate (n = 3), and results are reported as mean ± SD with error bars. The relative standard deviation (RSD) was found to be below 5%, indicating excellent experimental precision and sensor reproducibility with minimal signal fluctuation. For reusability testing, modified electrodes were rinsed with deionized water and ethanol, retaining ~95% of their initial response after five DPV cycles, confirming good operational stability.

The stability was probed to assess the sensor's resilience during storage. Devices were stored under ambient conditions, and their performance was benchmarked weekly against a fresh ACh standard. The sensor retained 90% of its initial signal after 7 days and 85% after 14 days, subsequently reaching a stable plateau with no further significant degradation over the following three weeks (Fig. 6d). This decay profile suggests a minor initial relaxation or reorganization of the polymer matrix, after which the structure stabilizes. The excellent retention of activity after five weeks highlights the remarkable structural integrity of the ZnO·CuO NL–PPy composite and the enduring fidelity of the imprinted cavities, mitigating a common drawback of bio-based sensors prone to rapid denaturation. The observed 15% decline in signal intensity after two weeks is most

Table 2 Recovery data for the determination of acetylcholine in spiked human serum samples (n = 3)

Conc. spiked	Found	Recovery (%)	RSD (n = 3) (%)
20 pM	20.2 pM	101%	0.7
500 nM	490 nM	98%	1.42
50 mM	50.6 mM	101.2%	0.84

plausibly attributed to slight oxidative aging or surface relaxation of the PPy matrix rather than ZnO·CuO nanoleaf leaching, as evidenced by the subsequent stabilization of sensor response and retention of electrochemical activity.

3.9 Validation in a complex biological matrix

To unequivocally demonstrate the analytical utility and accuracy of our sensor in clinically relevant environments, we evaluated its performance in human serum, a complex matrix containing numerous potential interferents. Serum samples were obtained from the Health Centre, University of the Punjab, as per standard protocols and guidelines of the University. Ethical approval for the use of de-identified human serum samples was obtained from the Institutional Ethics Review Board (IERB), University of the Punjab, and informed consent was obtained from all participants. Serum samples were diluted 10-fold in phosphate buffer (pH 7.4) to mitigate matrix effects and were then analyzed using the standard addition method to ensure accurate quantification and account for any inherent background signal. Aliquots of the diluted serum were spiked with known concentrations of acetylcholine at three levels (20 pM, 500 nM, and 50 mM) covering the sensor's entire dynamic range. The concentration of ACh in the spiked samples was determined from the measured DPV current and the established calibration curve.

As summarized in Table 2, the sensor demonstrated exceptional accuracy and reliability. The calculated recovery rates for the spiked ACh ranged from 98.0% to 101.2%, with relative standard deviations (RSD) below 1.5% for all replicates (n = 3). These near-quantitative recoveries provide compelling evidence of the sensor's high selectivity and robustness against fouling in a complex biological fluid. The successful application in human serum validates the primary advantage of our design: the synergy between the selective MIP and the electrocatalytic ZnO·CuO NLs creates an interface that is not only highly sensitive but also remarkably resistant to non-specific adsorption. This performance starkly contrasts with the inherent fragility of enzymatic biosensors in such matrices. Therefore, these results confirm the practical viability of our MIP-based sensor for the direct, rapid, and accurate detection of acetylcholine in real-world clinical samples.

4. Conclusion

In summary, we have engineered a novel biomimetic sensor through the synergistic integration of ZnO·CuO NLs within a MIP (PPy) matrix on a low-cost pencil graphite electrode. This design leverages the electrocatalytic properties of the nanoleaf heterostructure to enhance signal transduction and the precise molecular recognition of imprinting to achieve exceptional selectivity for acetylcholine. The resulting non-enzymatic sensor demonstrates unparalleled performance, boasting an ultra-low detection limit of 2.2 pM and a broad linear dynamic range spanning nine orders of magnitude (100 pM to 100 mM). The sensor's high specificity, validated both computationally and experimentally against key interferents, coupled with its successful application in human serum with excellent recovery rates, underscores its robustness in complex matrices. Furthermore, its remarkable reproducibility, long-term stability, and reusability confirm its practical viability. This work establishes a powerful, cost-effective, and reliable sensing platform that holds significant immediate promise for the development of point-of-care diagnostic devices for the early detection of cancers and neurodegenerative disorders linked to dysregulated cholinergic signaling.

Conflicts of interest

The authors declare no conflict of interest.

Data availability

The data that support the findings of this study have been included in the manuscript.

Acknowledgements

The authors of this work are very grateful to the Pakistan Science Foundation (PSF) of Pakistan for financial support under project no. PSF/Res/P-CIIT/Med (477) and the Ministry of Science and Technology of the Government of Pakistan for providing financial support through the "Establishment of Centre for Advanced Technologies in Biomedical Material" development grants as part of the Government of Pakistan's knowledge economy initiative.

References

1 R. Webster, in *Neurotransmitters, Drugs and Brain Function*, John Wiley & Sons, Ltd, 2001, pp. 117–136.
2 X. Gu and X. Wang, *Anal. Biochem.*, 2021, **632**, 114381.
3 F. T. C. Moreira, M. G. F. Sale and M. Di Lorenzo, *Biosens. Bioelectron.*, 2017, **87**, 607–614.
4 S. Soylemez, V. Dolgun and S. Özçubukçu, *Microchem. J.*, 2023, **193**, 109099.
5 N. H. B. Ho, D. L. Glasco, R. N. Sopp and J. G. Bell, *ECS Trans.*, 2022, **109**, 29.
6 Z.-R. Chen, J.-B. Huang, S.-L. Yang and F.-F. Hong, *Molecules*, 2022, **27**, 1816.
7 S. Chanda and H. M. Mehendale, in *Encyclopedia of Toxicology*, ed. P. Wexler, Elsevier, New York, 2nd edn, 2005, pp. 33–34.

8 T. P. Song and E. R. Spindel, *J. Pharmacol. Sci.*, 2008, **106**, 180–185.
9 K. Cheng, R. Samimi, G. Xie, J. Shant, C. Drachenberg, M. Wade, R. J. Davis, G. Nomikos and J.-P. Raufman, *Am. J. Physiol.*, 2008, **295**, G591–G597.
10 P. Song, H. S. Sekhon, Y. Jia, J. A. Keller, J. K. Blusztajn, G. P. Mark and E. R. Spindel, *Cancer Res.*, 2003, **63**, 214–221.
11 J. P. Muñoz and G. M. Calaf, *Biology*, 2023, **12**, 1418.
12 A. Novotny, K. Ryberg, J. Heiman Ullmark, L. Nilsson, A. Khorram-Manesh, S. Nordgren, D. S. Delbro and G. Nylund, *Scand. J. Gastroenterol.*, 2011, **46**, 446–455.
13 P. H. Nguyen, Y. Touchefeu, T. Durand, P. Aubert, E. Duchalais, S. Bruley des Varannes, C. Varon, M. Neunlist and T. Matysiak-Budnik, *Tumor Biol.*, 2018, **40**, 1010428318799028.
14 A. S. Sacramento, F. T. C. Moreira, J. L. Guerreiro, A. P. Tavares and M. G. F. Sales, *Mater. Sci. Eng., C*, 2017, **79**, 541–549.
15 K. M. Mitchell, *Anal. Chem.*, 2004, **76**, 1098–1106.
16 K. Phasuksom, N. Thongwattana, N. Ariyasajjamongkol and A. Sirivat, *J. Electroanal. Chem.*, 2024, **964**, 118337.
17 Y. Zhang, F. D. Tingley, E. Tseng, M. Tella, X. Yang, E. Groeber, J. Liu, W. Li, C. J. Schmidt and R. Steenwyk, *J. Chromatogr., B*, 2011, **879**, 2023–2033.
18 E. Lamy, L. Pilyser, C. Paquet, E. Bouaziz-Amar and S. Grassin-Delyle, *Talanta*, 2021, **224**, 121881.
19 G. Cannazza, M. M. Carrozzo, A. S. Cazzato, I. M. Bretis, L. Troisi, C. Parenti, D. Braghiroli, S. Guiducci and M. Zoli, *J. Pharm. Biomed. Anal.*, 2012, **71**, 183–186.
20 P. Świt, A. Pollap and J. Orzeł, *Top. Curr. Chem.*, 2023, **381**, 16.
21 Z. Song, Y. Zhou, X. Han, J. Qin and X. Tang, *J. Mater. Chem. B*, 2021, **9**, 1175–1188.
22 Z. Feng, H. N. Lim, I. Ibrahim and N. S. K. Gowthaman, *J. Mater. Chem. B*, 2023, **11**, 9099–9127.
23 R. R. Poolakkandy, N. A. Ramalakshmi, K. A. Padmalayam, R. G. Krishnamurthy and M. M. Menamparambath, *Sens. Diagn*, 2023, **2**, 726–735.
24 S. Baruah, B. Maibam, J. Jaiswal, A. Kumar and S. Kumar, *Sens. Diagn*, 2023, **2**, 1236–1248.
25 B. A. Hussein, A. A. Tsegaye, G. Shifera and A. M. Taddesse, *Sens. Diagn*, 2023, **2**, 347–360.
26 I. Zaman, A. Liaqat, S. Athar, A. Mujahid and A. Afzal, *J. Mater. Chem. B*, 2024, **12**, 5898–5906.
27 S. Ashraf, T. Hussain, S. Z. Bajwa, A. Mujahid and A. Afzal, *J. Mater. Chem. B*, 2024, **12**, 6905–6916.
28 I. G. David, D.-E. Popa and M. Buleandra, *J. Anal. Methods Chem.*, 2017, **2017**, 1905968.
29 Á. Torrinha, C. G. Amorim, M. C. B. S. M. Montenegro and A. N. Araújo, *Talanta*, 2018, **190**, 235–247.
30 N. Leibl, K. Haupt, C. Gonzato and L. Duma, *Chemosensors*, 2021, **9**, 123.
31 Y. Li, L. Luo, Y. Kong, Y. Li, Q. Wang, M. Wang, Y. Li, A. Davenport and B. Li, *Biosens. Bioelectron.*, 2024, **249**, 116018.
32 T. Zidarič, D. Majer, T. Maver, M. Finšgar and U. Maver, *Analyst*, 2023, **148**, 1102–1115.
33 H. F. EL Sharif, S. R. Dennison, M. Tully, S. Crossley, W. Mwangi, D. Bailey, S. P. Graham and S. M. Reddy, *Anal. Chim. Acta*, 2022, **1206**, 339777.
34 L. Moreira Gonçalves, *Curr. Opin. Electrochem.*, 2021, **25**, 100640.
35 M. M. Hussain, A. M. Asiri and M. M. Rahman, *Microchem. J.*, 2020, **159**, 105534.
36 R. Dennington, T. A. Keith and J. M. Millam, *GaussView 6*, 2019.
37 M. J. E. A. Frisch, G. W. Trucks, H. B. Schlegel, G. E. Scuseria, M. A. Robb, J. R. Cheeseman, G. Scalmani, V. P. G. A. Barone, B. Mennucci, G. A. Petersson, H. Nakatsuji, M. Caricato, X. Li, H. P. Hratchian, A. F. Izmaylov, J. Bloino, G. Zheng, J. L. Sonnenberg, M. Hada, M. Ehara, K. Toyota, R. Fukuda, J. Hasegawa, M. Ishida, T. Nakajima, Y. Honda, O. Kitao, H. Nakai, T. Vreven, J. A. Montgomery Jr., J. E. Peralta, F. Ogliaro, M. Bearpark, J. J. Heyd, E. Brothers, K. N. Kudin, V. N. Staroverov, R. Kobayashi, J. Normand, K. Raghavachari, A. Rendell, J. C. Burant, S. S. Iyengar, J. Tomasi, M. Cossi, N. Rega, J. M. Millam, M. Klene, J. E. Knox, J. B. Cross, V. Bakken, C. Adamo, J. Jaramillo, R. Gomperts, R. E. Stratmann, O. Yazyev, A. J. Austin, R. Cammi, C. Pomelli, J. W. Ochterski, R. L. Martin, K. Morokuma, V. G. Zakrzewski, G. A. Voth, P. Salvador, J. J. Dannenberg, S. Dapprich, A. D. Daniels, Ö. Farkas, J. B. Foresman, J. V. Ortiz, J. Cioslowski and D. J. Fox, *Gaussian 16*, 2016.
38 T. Lu and F. Chen, *J. Comput. Chem.*, 2012, **33**, 580–592.
39 W. Humphrey, A. Dalke and K. Schulten, *J. Mol. Graphics*, 1996, **14**, 33–38.
40 L. Fang, B. Zhang, W. Li, X. Li, T. Xin and Q. Zhang, *RSC Adv.*, 2014, **4**, 7167–7173.
41 S. Sun, X. Zhang, Y. Sun, S. Yang, X. Song and Z. Yang, *Phys. Chem. Chem. Phys.*, 2013, **15**, 10904–10913.
42 D. V. Barsukov and I. R. Subbotina, *Russ. Chem. Bull.*, 2017, **66**, 1847–1853.
43 M. Mecozzi, E. Pietrantonio, M. Amici and G. Romanelli, *Analyst*, 2001, **126**, 144–146.
44 J. R. Mejia-Bernal, C. Gómez-Solís, I. Juárez-Ramírez, G. Ortiz-Rabell and L. A. Díaz-Torres, *J. Mater. Sci.: Mater. Eng.*, 2025, **20**, 38.
45 A. Kargar, Y. Jing, S. J. Kim, C. T. Riley, X. Pan and D. Wang, *ACS Nano*, 2013, **7**, 11112–11120.
46 M. Caglar and S. Ruzgar, *J. Alloys Compd.*, 2015, **644**, 101–105.
47 M. Nesa, M. Sharmin and A. H. Bhuiyan, *Mater. Sci. Semicond. Process.*, 2021, **122**, 105479.
48 P. Phogat, Shreya, R. Jha and S. Singh, *ECS J. Solid State Sci. Technol.*, 2023, **12**, 034004.
49 V. Shrivastav, Mansi, P. Dubey, V. Shrivastav, A. Kaur, M. Hołdyński, A. Krawczyńska, U. K. Tiwari, A. Deep, W. Nogala and S. Sundriyal, *Sci. Rep.*, 2023, **13**, 20675.
50 Z. Masood, H. Muhammad and I. A. Tahiri, *Electrochem*, 2024, **5**, 57–69.
51 R. D. Crapnell and C. E. Banks, *Talanta Open*, 2021, **4**, 100065.
52 Y. Fan, W. Qiao, W. Long, H. Chen, H. Fu, C. Zhou and Y. She, *Spectrochim. Acta, Part A*, 2022, **274**, 121033.

53 M. Rezaei, H. A. Panahi, S. Nasrollahi, E. Moniri and N. Torabi Fard, *Sep. Sci. Technol.*, 2023, **58**, 1516–1526.
54 S. Suryana, Mutakin, Y. Rosandi and A. N. Hasanah, *Molecules*, 2021, **26**, 1891.
55 T. Lu and Q. Chen, *Chem.: Methods*, 2021, **1**, 231–239.
56 H. M. Badran, K. M. Eid, H. O. Al-Nadary and H. Y. Ammar, *Molecules*, 2024, **29**, 2168.
57 E. S. Mozafari, M. T. Baei and E. T. Lemeski, *Sci. Rep.*, 2025, **15**, 23034.
58 L. Wang, X. Chen, C. Liu and W. Yang, *Sens. Actuators, B*, 2016, **233**, 199–205.
59 E. Aynacı, A. Yaşar and F. Arslan, *Sens. Actuators, B*, 2014, **202**, 1028–1036.
60 N. Chauhan, J. Narang and U. Jain, *Analyst*, 2015, **140**, 1988–1994.
61 N. Chauhan, S. Chawla, C. S. Pundir and U. Jain, *Biosens. Bioelectron.*, 2017, **89**, 377–383.
62 C. Murugan, N. Murugan, A. K. Sundramoorthy and A. Sundaramurthy, *ACS Appl. Nano Mater.*, 2020, **3**, 8461–8471.
63 N. Chauhan, S. Tiwari, T. Narayan and U. Jain, *Appl. Surf. Sci.*, 2019, **474**, 154–160.
64 N. Chauhan, S. Balayan and U. Jain, *Synth. Met.*, 2020, **263**, 116354.
65 N. Sattarahmady, H. Heli and R. D. Vais, *Biosens. Bioelectron.*, 2013, **48**, 197–202.
66 H. Beitollahi, M. Safaei and S. Tajik, *Electroanalysis*, 2019, **31**, 1135–1140.
67 A. C. Anithaa, K. Asokan and C. Sekar, *J. Taiwan Inst. Chem. Eng.*, 2018, **84**, 11–18.
68 P. Balasubramanian, T. S. T. Balamurugan, S.-M. Chen, T.-W. Chen and T. Sathesh, *ACS Sustainable Chem. Eng.*, 2018, **7**, 5669–5680.
69 P. Balasubramanian, T. S. T. Balamurugan, S.-M. Chen and T.-W. Chen, *ACS Sustainable Chem. Eng.*, 2019, **7**, 7642–7651.
70 M. Y. Emran, M. A. Shenashen, A. El Sabagh, M. M. Selim and S. A. El-Safty, *Colloids Surf., B*, 2022, **210**, 112228.
71 M. M. Hussain, A. M. Asiri, M. A. Hasnat, S. B. Aoun and M. M. Rahman, *ChemistrySelect*, 2022, **7**, 202200079.